

Mg₂Si and Ca₂Si semiconductors for photovoltaic applications: Calculations based on density-functional theory and the Bethe-Salpeter equation

Vinod Kumar Solet * and Sudhir K. Pandey †

*School of Mechanical and Materials Engineering,
Indian Institute of Technology Mandi, Kamand – 175075, India*
(Dated: March 4, 2025)

We conduct a comprehensive assessment of the electronic and optical properties, as well as photovoltaic (PV) performance parameters, for low-cost, nontoxic Mg₂Si and Ca₂Si using density-functional theory (DFT) and Bethe-Salpeter equation (BSE) based methods. The band-gap for Mg₂Si (Ca₂Si) is found to be in the range of 0.25-0.6 (0.57-0.96) eV when PBE, PBEsol and mBJ functionals are used. Effective masses at last-filled valence and first-empty conduction bands are in the range of 0.14-0.17 (1.17-1.25) m_e and 0.27-0.29 (0.3-0.41) m_e , respectively. In the *independent-particle* approximation (IPA), the real and imaginary parts of dielectric function show maximum values of ~ 50 (16.3) at ~ 2.6 (1.0) eV and ~ 61 (16.2) at ~ 3.24 (3.4) eV, respectively. Within BSE, these respective values change to ~ 59 (17) at ~ 2.5 (0.86) eV and ~ 65 (16.6) at ~ 2.68 (3.1) eV. The excitonic effect is found to be crucial in understanding the experimental optical spectra of Mg₂Si. However, this effect is relatively weaker in Ca₂Si. In solar spectrum active region, the highest absorption coefficient and lowest reflectivity change from ~ 1.5 (0.75) $\times 10^6$ cm^{-1} and ~ 0.39 (0.3) in IPA, respectively, to ~ 1.6 (0.88) $\times 10^6$ cm^{-1} and ~ 0.41 (0.27) in BSE. Present study highlights the importance of different levels of theoretical approximations for obtaining the optical spectroscopy data of silicides with a high level of accuracy. Finally, we have evaluated PV efficiency by using spectroscopic limited maximum efficiency (SLME) calculation. On the top of radiative recombination, we have also incorporated non-radiative carrier recombination at a defect trap state via Shockley-Read-Hall (SRH) mechanism to evaluate the efficiency. Among the studied defects, the interstitial Mg (Si) is identified as the most stable in Mg₂Si (Ca₂Si), and this provides SRH lifetime of ~ 2 μs (11.3 ms). The estimated maximum SLME using BSE absorption spectrum is ~ 1.3 (31.2)%, which decreases to ~ 1.2 (28.5)% due to SRH recombination. The present study suggests that Ca₂Si (Mg₂Si) is a potential candidate for single-junction (bottom cell in multi-junction) thin-film PV devices.

I. INTRODUCTION

Semiconductors are playing a pivotal role in the current technological revolution. The spectroscopy of light-matter interaction in semiconductors is an intriguing topic in both modern research and industrial applications [1]. One of the most significant technologies for generating renewable energy is PV solar cells. Essentially, a common question when designing solar cells is the amount of incident sunlight that the optically active materials can absorb, as well as how to adjust these materials to absorb more light and generate a large number of electron-hole ($e-h$) pairs. It also becomes critical to understand how to optimize materials that efficiently convert these $e-h$ pairs into useful electricity. The response function calculation [2] is a fundamental study that particularly provides a theoretical spectroscopic analysis of PV semiconducting materials.

The past few decades have seen the thorough use of *first principles* based DFT and Fermi's golden rule to investigate the optical absorption of many semiconductors [3, 4]. Unfortunately, DFT calculations do not describe the key aspect of optical absorption, which is $e-h$ interaction, because they only deal with single-particle

states [5]. An absorbing photon excites a valence electron into the conduction band, leaving a hole behind in the valence band; thus, $e-h$ pair is created. Single-particle theories treat this created $e-h$ pair as independent, non-interacting particles. These theory-based optical spectra, estimated within *independent-particle* approximation (IPA), often have significant deviations from experiment [6–8]. However, for an interacting system, it has been assumed that the bound states of an excited *quasielectron* and a *quasihole* (excitons) are the missing ingredients for a significant comparison between the theoretical and experimentally measured optical spectra [4, 9–11]. To obtain an accurate optical response, one must consider the *screened* Coulomb interaction in the excited $e-h$ pairs. In particular, the Bethe-Salpeter equation (BSE) [12], an effective two *quasiparticle* equation for polarizability [4, 13], can be solved using many-body perturbation theory (MBPT) based on Green's function approach in an *ab initio* framework [6, 14].

Efficient solar devices do not always rely on optical parameters [15]; they also depend on the type of band-gap as well as various solar cell parameters [15–17]. Some successful theoretical studies using the *first principles* approach have identified new solar materials with a high power conversion efficiency [18, 19]. The Shockley-Queisser (SQ) model [20] is used widely to predict the theoretical efficiency of single-junctional solar cells. In this approach, the efficiency is directly related

* vsolet5@gmail.com

† sudhir@iitmandi.ac.in

to the band-gap of the light-absorbing layer, while other properties such as optical absorption, carrier transport, and lifetimes are assumed to be ideal. The SQ-model can be further improved by considering optical absorption in SLME model [15]. Generally, any excited or injected charge carrier that does not leave the semiconducting material can undergo various types of recombination [21, 22]. The difference between SQ limit or SLME and the efficiencies of actual solar devices arise mainly from additional irreversible processes, such as non-radiative $e-h$ recombination. Therefore, we have also calculated the efficiency by including losses of $e-h$ pairs inside solar absorbers both from radiative and non-radiative processes [17, 23]. The current density due to radiative recombination can be easily estimated, but one needs to know about defect properties in semiconductors to determine non-radiative current density [24, 25]. In PV solar devices, the trap states or recombination centers of a defect in the band-gap help photo-excited carriers to recombine non-radiatively, also commonly referred to as SRH recombination [22, 26, 27]. In our calculation, the SRH carrier lifetime limits the efficiency based on the electronic dispersion, optical absorption, and thermodynamical properties of defects of an absorbing material.

This paper chooses solar materials based on their environmental friendliness, lower cost, availability on earth, and non-toxic characteristics. Silicon-based materials can be one of the best choices used in solar cells. In this category, researchers gain a lot of interest in semiconducting silicides [28, 29] in thin-film solar technology due to their high optical absorbance [30, 31]. For instance, the Mg_2Si semiconductor [29] is one of the silicides that has been studied the most. It has experimental indirect band gaps in the range of 0.61 to 0.8 eV [32–38] and a large absorption coefficient from reflectance measurements of $\sim 3 \times 10^5 \text{ cm}^{-1}$ at 2.5 eV of visible energy [33]. However, in theory, the indirect band gaps for Mg_2Si lie in the range of ~ 0.118 -0.53 eV [39–42]. Various other experiments such as spectroscopic ellipsometry [35] and reflectance [43–45] measurements were performed to obtain optical properties for Mg_2Si . Another same class of silicide is cubic Ca_2Si , which is found to have theoretical direct band gaps of 0.56 [46] and 1.16 [47] eV from DFT and GW approximation, respectively. However, the full investigation of both silicides for solar applications has yet to be done, and the appropriate band gaps provide a promising outlook for future research into their solar application properties. But the available theoretical gaps are not consistent with each other. So, it makes sense to estimate a band gap for Mg_2Si that is similar to what has been observed in experiments. The band gap calculation in DFT depends a lot on the exchange and correlation (XC) potentials. One thing also to keep in mind is that we work here on the theoretical (electronic and optical properties) as well as application aspects for these two silicides. Therefore, we first validate the different approximations based on IPA and MBPT for theoretical aspect in Mg_2Si using the available experimental data. Based

on this validation, we explore its practical applications in PV technology. We then apply the same methodology to Ca_2Si , despite the lack of experimental data, to provide insights into its potential applications.

Therefore, this study includes a *first principles* analysis using two functionals (PBE, PBEsol) and mBJ potential to estimate the electronic and optical properties for Mg_2Si and Ca_2Si , with the aim of optimizing their solar efficiency. The predicted fundamental band-gaps range for Mg_2Si and Ca_2Si are ~ 0.25 -0.60 eV and ~ 0.57 -0.96 eV, respectively. The evaluated optical gap from mBJ is ~ 2.45 and 0.96 eV, respectively. We also evaluate the density of states effective masses of charge carriers at high-symmetric points. The optical properties are calculated without and with considering $e-h$ interaction in IPA (PBE, mBJ and PBE+scissor) and BSE methods, respectively. All optical parameters show broad spectra in the visible light. However higher absorption can't guarantee an efficient single-junction solar cell. Therefore, we estimate the efficiency by incorporating various $e-h$ recombination processes. At 300 K, the highest predicted efficiency using BSE absorption coefficient by explicitly considering only radiative recombination (SLME) is $\sim 31.2\%$ for Ca_2Si and $\sim 1.3\%$ for Mg_2Si . The point-defect calculation mainly yields the SRH lifetime required to calculate the non-radiative recombination. Among the defects analyzed, the interstitial Mg (Si) defect is found to be most stable in Mg_2Si (Ca_2Si). Accounting for thermodynamic properties of defect, the SRH lifetime is estimated to be $\sim 2 \mu s$ (11.3 ms). Consequently, the maximum possible trap-limited conversion (TLC) efficiency at 300 K using BSE absorption spectra is predicted to be ~ 1.2 (28.5)%. As a result, Ca_2Si can be used to make thin-film single-junction solar cells. Moreover, narrow-gap Mg_2Si , with its high absorption is a suitable PV material for fabricating a bottom layer in multi-junction cell.

II. COMPUTATIONAL DETAILS

Electronic structure calculation was performed by using of augmented plane wave plus local orbitals (APW+lo) method within DFT as implemented in WIEN2k [48] code. The muffin-tin sphere radii (R_{MT}) value was kept fixed to 2.5 Bohr for all atoms. Also, a $10 \times 10 \times 10$ \mathbf{k} -mesh size and convergence criteria of 10^{-4} Ry/cell for total energy had to be considered for solving the Kohn-Sham (KS) equation. Further two different functionals, *i.e.*, PBE [49] and PBEsol [50] were considered as a XC part of the KS equation. The inherent band-gap underestimation of DFT was corrected by the using of Tran-Blaha modified Becke-Johnson (TB-mBJ) potential [51].

The optical dielectric function, at IPA level, was calculated using the WIEN2k code. The *independent-particle* polarizability, which uses KS orbitals and eigenvalues, required for the calculation of dielectric function was estimated within the random-phase approximation (RPA), which is also known as the KS-RPA. Meanwhile,

the \mathbf{k} -mesh was built into a large 5000 \mathbf{k} -points over the full Brillouin zone to obtain the momentum matrix elements. The Lorentzian broadening value of 50 meV was used. The components of an effective mass tensor using the degenerate perturbation approach were obtained by the `mstar` code implemented in `WIEN2k` software [52]. Effective mass calculation in this framework is very sensitive to the momentum matrix elements that contain upper energy bands. Thus, these matrix elements were obtained within the maximum energy of 10 Ry, which corresponds to the 236 and 164 bands for Ca_2Si and Mg_2Si , respectively. The tolerance parameter of degeneracy energy was used as 10^{-5} Ha.

Optical properties including e - h interactions using MBPT were estimated from the all-electron full-potential `exciting` code through the solution of BSE within the Tamm-Dancoff approximation (TDA) [14]. Initially, the ground state eigenenergies and eigenstates from PBE functional were obtained at a \mathbf{k} grid of $12 \times 12 \times 12$. A $5 \times 5 \times 5$ \mathbf{k} -mesh size shifted by (0.097, 0.273, 0.493) was employed for the BSE calculation. For screening calculation, a $5 \times 5 \times 5$ \mathbf{q} -mesh size was used. We used 50 empty states for both silicides to construct the excitonic Hamiltonian. The energy threshold for including the local field effects in the excited states, $|\mathbf{G} + \mathbf{q}|_{max}$, was taken into account upto a cutoff of $3.0 a_0^{-1}$. A Lorentzian lifetime broadening of 50 meV was applied to the optical spectra to obtain comparable results with the experiment. For both compounds, 100 empty states were adopted in the RPA calculation for the *screened* Coulomb interaction between electron and hole. A scissor shift of 0.55 and 0.4 eV was applied to the optical spectra in order to mimic the *quasiparticle* (QP) correction in Mg_2Si and Ca_2Si , respectively. Finally, the considered transition space includes all occupied and the first 20 unoccupied bands in order to diagonalize the BSE Hamiltonian for both compounds.

The calculation of point defects were performed using DFT within $2 \times 2 \times 2$ size of supercell containing of total 96 atoms in pristine structure for both compounds using the `WIEN2k` code [48]. The defects were simulated by removing and/or adding the constituent atoms from and/or to the pristine structure. The PBE functional was used [49], and BZ was sampled with a \mathbf{k} -mesh size of $4 \times 4 \times 4$. The self-consistency calculations continued until the structure was fully relaxed through structural optimization.

III. RESULTS AND DISCUSSION

A. Electronic properties

Here, the electronic and optical properties of Mg_2Si and Ca_2Si compounds have been investigated in their anti-fluorite structure with a space group of $\text{Fm}\bar{3}\text{m}$ (No. 225). The used value of lattice parameters in the entire calculations for Mg_2Si and Ca_2Si is 6.35 Å, and

7.16 Å, respectively. The value of lattice parameter for Mg_2Si is very close to the experimental value [53]. The primitive unit cell of both compounds consists of three atoms, in which one Si atom is located at the (0, 0, 0) and two Mg (Ca) atoms are situated at the position of (0.25, 0.25, 0.25) and (0.75, 0.75, 0.75). All these above structural parameters are directly taken from the `AFLOW` database [54].

The calculation of the band gap from electronic dispersion offers a promising method for finding suitable PV materials. Optical processes have been related to vertical (or direct) transitions and number of photo-excited electrons in conduction bands strongly depends on the band gap. The optical dielectric function in Eq. (1) is also directly related to the eigenvalues of occupied and unoccupied states. Thus both direct and indirect gaps are critical for PV device performance, making it essential to provide an accurate predictions for gaps. The DFT band structure gives accurate information regarding the shape of energy bands, but a major problem with this theory is that it generally underestimates the band-gap of semiconductors or insulators. This is due to its improper treatment of the XC potential, which includes factors such as the self-interaction error in GGA or LDA and the absence of density-functional derivative discontinuity in the XC energy [55]. In order to properly handle the exchange potential, the mBJ potential [51] is used to obtain the best possible band gaps for both silicides, as this approach is known to yield more precise gaps commonly observed in many semiconductors [56, 57].

Therefore, the electronic dispersions for both silicides have been calculated from PBE & PBEsol functional, and mBJ potential, which are presented in Fig. 1. Table I summarizes the fundamental and optical band gaps obtained from the different functionals, along with the available experimental gaps for Mg_2Si . Unfortunately, experimental band gap is not available for cubic Ca_2Si . It is noticed that the band gap increases in the silicides by replacing the light Mg atom with a heavy Ca atom. In Fig. 1(a), Mg_2Si is found to be an indirect band gap semiconductor, where highest energy level of valence band (VB), ε_v , and lowest energy level of conduction band (CB), ε_c , are at Γ - and X-point, respectively. With PBE (PBEsol) the indirect gap is ~ 0.25 (0.16) eV, 59-69 (74-80)% smaller than the experimental gaps of ~ 0.61 -0.8 eV [32–38]. In contrast, an indirect gap of ~ 0.6 eV within mBJ aligns well with the experimental gaps. The estimated value of an optical gap at Γ -point from PBE (PBEsol) is ~ 1.92 (1.76) eV, while it is ~ 2.45 eV from mBJ. Reflectivity experiment at 77 K [33] and electro-reflectance measurement at room temperature [45] revealed an optical gap of ~ 2.17 and 2.27 eV, respectively. Next, from Fig. 1(b), Ca_2Si is a direct band gap semiconductor with a value of ~ 0.57 (0.52) eV at a X-point obtained from the PBE (PBEsol) functional, and the calculated gap from the mBJ potential is ~ 0.96 eV. The VB near Fermi energy (ε_F) seems to be less (more) dispersive in the direction of Γ -L (Γ -X) and X- Γ (X-W) for

TABLE I: Band gaps in eV from PBE, PBEsol and mBJ. The fundamental and optical (in brackets) gaps for Mg_2Si are compared to experiment values. For Ca_2Si , both fundamental and optical gaps are the same.

Methods	Mg_2Si	Ca_2Si
	Γ -X (Γ - Γ)	X-X
PBE functional	0.25 (1.92)	0.57
PBEsol functional	0.16 (1.76)	0.52
mBJ potential	0.60 (2.45)	0.96
Experimental	0.61-0.8 [32–38] (2.17-2.27 [33, 45])	Not available

Mg_2Si and Ca_2Si , respectively. These behaviors of bands in the respective directions are crucial for understanding the optical properties of both studied silicides. One can also notice in both materials that the PBE and PBEsol provide nearly comparable band structures. Therefore, further properties that depend on dispersion can be explained by taking only one of the functionals, and we consider PBE.

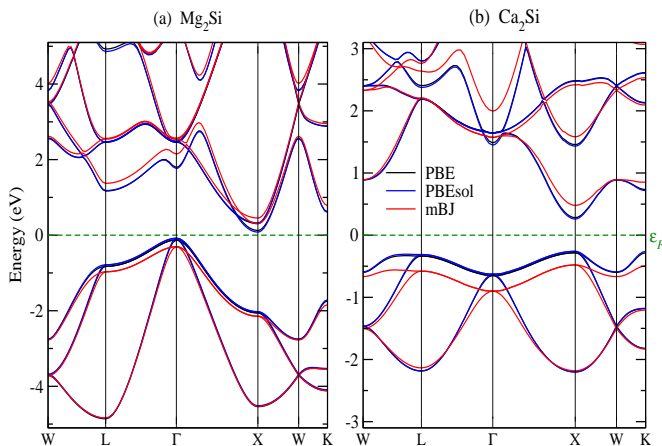


FIG. 1: Electronic band dispersion for (a) Mg_2Si and (b) Ca_2Si from PBE and PBEsol functionals, and mBJ potential.

The transition of electrons from filled to empty bands is critical to the interaction of light with semiconductors. As in Eq. (1), the success of such transitions depends on the number of available states as well as the transition probability of electrons from occupied to unoccupied states at a particular photon energy. Thus, in Fig. 2, the total density of states (TDOS) along with the partial density of states (PDOS) plots have been shown. Both compounds show a band gap near the ε_F , which is a nature of being semiconducting compounds. For Mg_2Si , one can notice the sharp rise in states at the topmost (bottom-most) region of the VB (CB), which is a good sign for solar materials. Except peak intensities, there is a slightly change in PBE states with the inclusion of mBJ potential. Two maximum peaks in the VB region are located around the energies of ~ -1.95 and ~ -4.17 eV. In the CB region, a largest peak is found around the energy of ~ 2.7 eV. Similarly, in Fig. 2(b) for Ca_2Si , there have

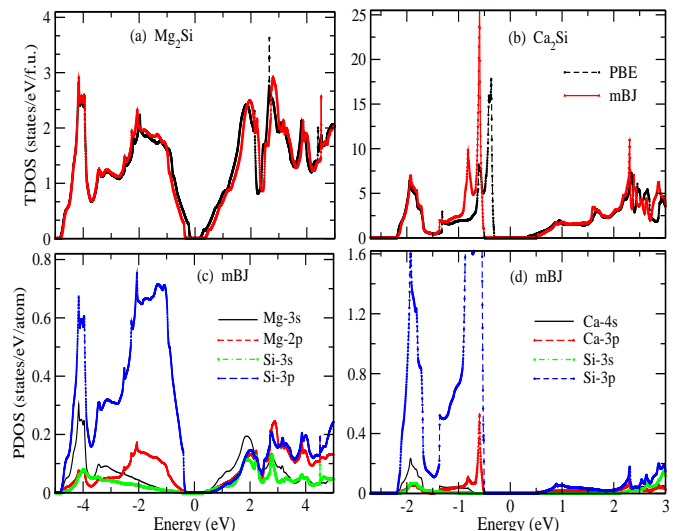


FIG. 2: Total/partial density of states (T/PDOS) plots for Mg_2Si and Ca_2Si .

been sharply increasing states in the vicinity of the ε_F on the VB side. These VB states are shifted by ~ 0.2 eV on the lower energy side by adding mBJ in PBE, while states in CB have not changed significantly. The maximal peaks in the VB and CB regions from PBE (mBJ) are situated at nearly -0.35 (0.6) eV and ~ 2.3 eV, respectively. The PDOS obtained from mBJ has been shown, in which the electronic states of VB are significantly contributed by the Si-3p and Si-3s orbitals, respectively, in the VB and CB regions. Similarly, in Fig. 2(d), the whole VB and CB regions are rich in Si-3p character with a low contribution from Ca-4s,3p states. The Si-3p and Ca-3p states in the VB and CB regions, respectively, have been responsible for creating the band gap and may also be actively involved in the photo-conversion process.

The effective mass of the charge carriers (electrons and holes) in the vicinities of ε_c and ε_v is of great importance for analyzing the carrier transport such as mobilities and the current density in the PV materials [52, 58]. The density of states effective mass (m_{dos}^*) of the charge carriers directly affect the electrical conductivity [59], and depletion width of the pn -junction solar cells based on intrinsic concentration [58, 60, 61]. Therefore, in Table II, the m_{dos}^* is calculated at high-symmetric points for the last filled VB and first empty CB in the vicinity of ε_F . The m_{dos}^* is obtained from the geometric mean of the principal components of the effective mass tensor (m_1^* , m_2^* , m_3^*), i.e., $\sqrt[3]{m_1^* \times m_2^* \times m_3^*}$ [52]. The m_{dos}^* at ε_v is observed to be ~ 0.14 - $0.17m_e$ and 1.17 - $1.25m_e$, whereas in ε_c , it is ~ 0.27 - $0.29m_e$ and ~ 0.30 - $0.41m_e$ for Mg_2Si and Ca_2Si , respectively. The estimated m_{dos}^* of electron for Mg_2Si at ε_c is well matched with previously available theoretical effective mass (m_{\perp}^*) of $0.25m_e$ [62]. The negative (positive) value of m_{dos}^* at VB (CB) corresponds to a hole (electron) effective mass [63]. The experimen-

TABLE II: Calculated density of states effective mass m_{dos}^* (units of free electron mass (m_e)) at high-symmetric points for the VB and the CB extrema of Mg_2Si and Ca_2Si .

Values of m_{dos}^* for Mg_2Si/Ca_2Si compound				
High-symmetric points	PBE functional		mBJ potential	
	VB	CB	VB	CB
W	0.28/0.70	0.79/0.60	0.30/1.19	0.77/0.57
L	0.51/0.64	0.22/0.65	0.56/0.91	0.24/0.66
Γ	0.14/0.50	0.13/0.20	0.17/0.80	0.16/0.64
X	-0.47/1.17	0.27/0.30	-0.50/1.25	0.29/0.41
K	-0.64/8.80	0.39/0.45	-0.69/-6.54	0.41/0.51

tal effective masses obtained by *Morris et al.* [34] are $0.47m_e$ (for electron) and $0.87m_e$ (for hole), while those by *Heller et al.* [38] are $0.5m_e$ (for electron) and $2.0m_e$ (for hole). In another study, *Udono et al.* [32] found effective masses of $0.57m_e$ (for electron) and $1.07m_e$ (for hole), while *Nolas et al.* [64] found $0.51m_e$ (for electron). In Table II, the m_{dos}^* of p -type carriers in VB is larger than that of n -type carriers (similar trend as observed in experiment), and this is because the slope of DOS below ε_F exceeds that above. One possible reason for the difference between the calculated and experimental m_{dos}^* would be that the calculated m_{dos}^* is \mathbf{k} -points dependent, whereas the reported experimental results provides the overall value for the materials. However, the values in Table II are in the range of experimental values. For an excellent PV materials, the effective mass should be low, which corresponds to high mobility of electrons/holes at the CB/VB and resultantly high conductivity. For a material, it is reported that excellent carrier mobility can be obtained by having an effective mass value lower than $0.5m_e$ in at least one direction [65, 66]. In Table II, at least one high-symmetric point has a m_{dos}^* value of less than $0.5m_e$; therefore, both compounds may have great charge mobilities in the vicinities of ε_v and ε_c .

B. Optical properties

The operation and performance of solar devices are greatly affected by the optical properties of the underlying compound. Basically, these properties are obtained from the response function calculations in terms of frequency and wave vector dependent complex dielectric function $\epsilon(\omega)$. This has two contributions, which are due to inter-band and intra-band transitions. The contribution by the intra-band transitions is only significant for metals. The inter-band transitions are further classified as direct and indirect transitions. Here, the indirect inter-band transitions, which involve phonon scattering and are expected to contribute not much to $\epsilon(\omega)$ [67], are ignored. In this paper, the imaginary part of the dielectric function $\epsilon_2(\omega)$ is calculated at various levels of approximation. First, in IPA by the sum over indepen-

dent transitions between occupied (ν) and unoccupied (c) eigenstates of a one-particle Hamiltonian one defines

$$\epsilon_2^{IPA}(\omega) = \frac{Ve^2}{2\pi\hbar\omega^2m^2} \sum_{\nu c} \int d^3\mathbf{k} \left| \langle \nu\mathbf{k} | \mathbf{p} | c\mathbf{k} \rangle \right|^2 \times f(\nu\mathbf{k}) [1 - f(c\mathbf{k})] \delta(\varepsilon_{c\mathbf{k}} - \varepsilon_{\nu\mathbf{k}} - \hbar\omega) \quad (1)$$

where $\hbar\omega$ is the incident photon energy, V is the unit cell volume, \mathbf{p} is the momentum operator, and $f(\nu\mathbf{k})$ indicates the Fermi-distribution function. The δ function implies that the absorption occurs at energy eigenvalue differences ($\varepsilon_{c\mathbf{k}} - \varepsilon_{\nu\mathbf{k}}$). The estimation of matrix elements of momentum operator is performed separately over the muffin-tin and the interstitial regions. A complete description of the evaluation of these matrix elements can be found in the paper of *Draxl et al.* [68].

On the other hand, this method does not consider interacting e - h pairs and local field effects, which modify the overall shape of the optical dielectric function in a quite significant way. These changes can be made within the BSE approach on the top of DFT band structure from the MBPT [4, 14]. In practice, the BSE is mapped onto an eigenvalue problem for an effective two QP excitonic Hamiltonian H^{BSE} [6, 69];

$$\sum_{\nu'c'\mathbf{k}'} H_{\nu c\mathbf{k},\nu'c'\mathbf{k}'}^{BSE} A_{\nu'c'\mathbf{k}'}^\lambda = E^\lambda A_{\nu c\mathbf{k}}^\lambda \quad (2)$$

where $\nu c\mathbf{k}$ is an elementary excitation taking place from ν to c state at a particular \mathbf{k} -point in the IBZ. The eigenvalues E^λ correspond to the energy of coupled e - h excitation, whereas the eigenvectors $A_{\nu c\mathbf{k}}^\lambda$ is the excitation state in terms of coupling between λ^{th} e - h pair generated by $\nu\mathbf{k} \rightarrow c\mathbf{k}$ transitions. In two-particle interaction, the H^{BSE} is basically sum of the two terms as follows:

$$H^{BSE} = (\varepsilon_{c\mathbf{k}} - \varepsilon_{\nu\mathbf{k}} + \Delta) \delta_{cc'} \delta_{\nu\nu'} \delta_{\mathbf{k}\mathbf{k}'} + \Xi_{\nu c\mathbf{k},\nu'c'\mathbf{k}'} \quad (3)$$

The first term is the diagonal term that describes the transitions within the IPA with QP corrections. In BSE calculations, it is common to adopt the scissor operator to simulate the self-energy (or QP) corrections. Thus, to correct the band gap profile, we simply apply a rigid shift on the CB, known as scissor correction (Δ), which adjusts the optical gap of DFT calculation to mBJ. The second term is known as the effective e - h interaction kernel, and written for spin-singlet excitons (when spin is not explicitly treated) [14] as: $\Xi_{\nu c\mathbf{k},\nu'c'\mathbf{k}'} = 2\Xi_{\nu c\mathbf{k},\nu'c'\mathbf{k}'}^{exc} + \Xi_{\nu c\mathbf{k},\nu'c'\mathbf{k}'}^{dir}$. The first one is the short range *exchange* or unscreened Coulomb repulsion of vanishing wavevector ($\mathbf{q} \rightarrow 0$) mediated by the bare Coulomb potential. The second one is direct statically *screened* Coulomb attraction of a negatively charged electron in CB and a positively charged hole in VB [14] and responsible for the creation of the excitons. Within the TDA, the coupling between the resonant and anti-resonant components of H^{BSE} has been excluded [14]. Finally in optical limit ($\mathbf{q} \rightarrow 0$), the imaginary part of macroscopic dielectric

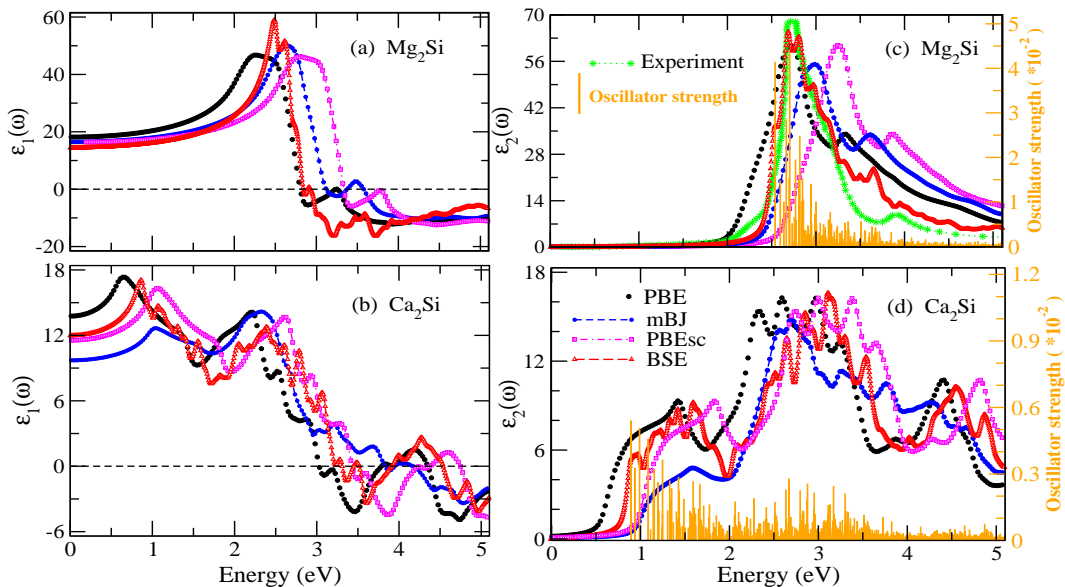


FIG. 3: Calculated real $\epsilon_1(\omega)$ and imaginary $\epsilon_2(\omega)$ parts of the dielectric function from IPA (PBE, PBE+scissor (PBEsc), and mBJ) and Bethe-Salpeter equation (BSE). In sub-figure (c), the experimental spectrum [33] for Mg_2Si is shown for comparison. The oscillator strength of individual BSE excitations in (c) & (d) is indicated by the vertical orange line.

function can be written as;

$$\epsilon_2^{BSE}(\omega) = \lim_{\mathbf{q} \rightarrow 0} \frac{8\pi^2}{\Omega q^2} \sum_{\lambda} \left| \sum_{\nu c \mathbf{k}} A_{\nu c \mathbf{k}}^{\lambda} \langle \nu \mathbf{k} | e^{-i\mathbf{q} \cdot \mathbf{r}} | c \mathbf{k} \rangle \right|^2 \times \delta(E^{\lambda} - \omega) \quad (4)$$

where Ω is the crystal volume. The square modulus of coupling of different e - h pair configurations $|\nu c\rangle$ in excitation state λ is known to be the oscillator strength in the optical spectrum. Equation (4) should be compared with Eq. (1); the differences between them are attributed to change in excitation energies (from $(\epsilon_c - \epsilon_{\nu})$ to E^{λ}), as well as, importantly, the coefficients A^{λ} , which enable the interpretation of spectra in terms of the mixing of formerly independent transitions.

The real part of dielectric function $\epsilon_1(\omega)$ can be obtained from the Kramers-Kronig (KK) relation [68, 70] as:

$$\epsilon_1(\omega) = 1 + \frac{2}{\pi} \int_0^{\infty} \frac{\epsilon_2(\omega') \omega' d\omega'}{\omega'^2 - \omega^2} \quad (5)$$

For a good accuracy of $\epsilon_1(\omega)$ calculation, one needs to take good representation of $\epsilon_2(\omega)$ up to high energies. In IPA calculation, $\epsilon_2(\omega)$ is calculated up to 100 eV and also this value used as a truncation energy in Eq. (5). Finally, the other optical parameters such as refractive index, absorption coefficient, and reflectivity can be easily obtained [68, 70].

It is important to note that the thermoelectric transport properties can be explained in better way by considering the band-gap correction on the different XC

functionals [71–73]. Both thermoelectric and PV transport properties are highly dependent upon electronic band structures. Thus, a reliable result of PV properties can be obtained with the scissor correction value on PBE functional. This value for Mg_2Si and Ca_2Si is used to be 0.55 eV and 0.4 eV, respectively, which is the difference between the optical band gap of mBJ and PBE calculations.

Therefore, in this section, we discuss the optical spectra of both silicides using different methods within IPA (PBE, PBE with scissor (PBEsc), and mBJ). The dielectric function, in Fig. 3, estimated within the IPA is compared to the ones considering many-body excitonic effects by solving the BSE. In Fig. 3(a), the static electronic dielectric function $\epsilon_1(0)$ (or ϵ_{∞}) from PBE is obtained to be ~ 18 for Mg_2Si , which overestimates the experimental value of ~ 13 [33]. Additionally, the $\epsilon_1(0)$ from PBEsc (~ 15.6) and mBJ (~ 16.5) fails to address this overestimating tendency. However, the BSE method estimates this value of ~ 14.4 , which is more consistent with the experimental value. This macroscopic electronic ϵ_{∞} can be influenced by considering the approximation beyond TDA [5]. Further, the highest peak of $\epsilon_1(\omega)$ is observed to be in the visible energy region of ~ 2.5 eV. In Fig. 3(b), the obtained $\epsilon_1(0)$ values from PBE, PBEsc, and mBJ are ~ 13.8 , 11.5, and 9.7, respectively, for Ca_2Si . Including the e - h interaction in the PBE reduces the $\epsilon_1(0)$ to ~ 12 . In the ultraviolet (UV) energy region, the majority of the $\epsilon_1(\omega)$ is negative, which means both materials show metallic character in this energy spectrum [58].

In Fig. 3(c), the calculated $\epsilon_2(\omega)$ spectra together with the available experimental data by Scouler [33] from

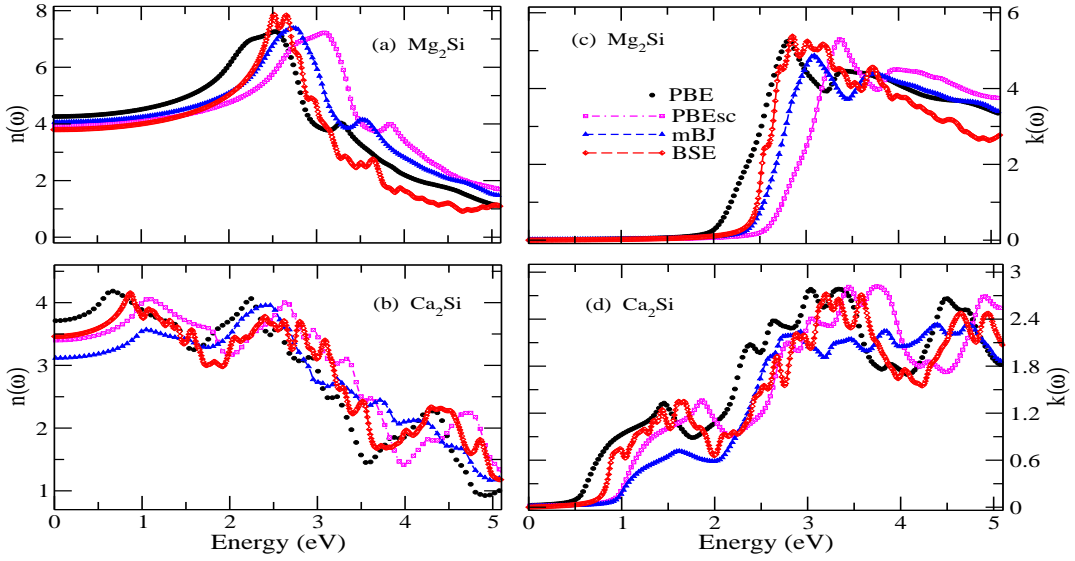


FIG. 4: The real $n(\omega)$ and imaginary $k(\omega)$ parts of refractive index comparing IPA (PBE, PBE+scissor (PBEsc), mBJ) with Bethe-Salpeter equation (BSE) for Mg_2Si and Ca_2Si compounds.

Reflectance measurement on Mg_2Si are presented. The tail that appears below the onset of respective absorption in both IPA and BSE is caused by the lifetime broadening effects, which resemble the self-energy contribution. The $\epsilon_2(\omega)$ obtained within the IPA with different methods reproduces mainly two bright peaks. The maximum of the first main peak appears at ~ 2.7 , 3.3 , and 3 eV from the PBE, PBEsc, and mBJ, respectively. For PBE, this peak nearly coincides with the first peak in the experimental $\epsilon_2(\omega)$ at ~ 2.73 eV. The spectra obtained from PBEsc show only a rigid shift relative to the PBE spectra, while the spectra within mBJ almost lie between the two. However, none of the three methods accurately reproduce spectra that can be compared with experimental results, as the oscillator strengths are not represented accurately. In Fig. 3(d), Ca_2Si exhibits multiple peaks of $\epsilon_2(\omega)$ from all methods, revealing several optical transitions for the particular dispersion of its ϵ_v and ϵ_c . In this figure, the $\epsilon_2(\omega)$ is increasing slowly from respective absorption edges to the first peak in all three IPA as well as BSE methods. All methods produce the highest peak in energy range of ~ 2.6 - 3.4 eV. One can see that the BSE calculation gives the red-shift on the PBEsc $\epsilon_2(\omega)$ spectrum, but the intensities of peaks are almost unchanged. The highest $\epsilon_2(\omega)$ within BSE lies in the visible energy region, which is ~ 16.7 at 2.1 eV. Until now, experimental optical spectra of Ca_2Si have not been available. On the other hand, in Fig. 3(c), the $\epsilon_2(\omega)$ spectrum calculated within BSE shifts towards lower energies compared to the PBEsc/mBJ spectrum. The shape of the spectrum is now improved and better described compared to the experiment, with a redistribution of transitions relative to the IPA results. However the BSE curve does not match the experimental data below the direct gap energy (2.45 eV) due to the exclusion of indirect transitions in the calcula-

tion. It shows fairly good agreement with the experimental counterpart at ~ 2.73 eV, with the calculated magnitude for BSE being ~ 65 compared to the experimental value of 68 . A large excitonic effect is observed in Mg_2Si than Ca_2Si , particularly at the optical gap edge. This may be due to the large optical band gap of Mg_2Si than Ca_2Si . Above ~ 3.3 eV in the UV energy region, there is a notable discrepancy between the BSE and experimental spectra. This may be due to the current calculations not considering the off-diagonal elements in the screening matrix [74], frequency-dependent (dynamical) screening [75], and electron-phonon coupling or polaronic excitation effects [76]. The well amplified energy peak from BSE at 2.54 eV is almost concealed in the Mg_2Si experimental spectrum. This could be due to two factors: a lower broadening value of 50 meV used in calculation, or the technique used to extract the experimental spectrum. In the latter case, Scouler [33] deduced the $\epsilon_2(\omega)$ from KK analysis of the reflectance data, which was measured only up to 11 eV. To perform a much more accurate KK transform, one must use the reflectance spectrum up to high photon energies. To produce a high-energy portion of the reflectance data, Scouler used a parameter-based tail function. However, he suggested that the positions and magnitudes of peaks can influence the choice of tail function [33], which complicates direct comparisons with theoretical results.

In order to gain a deeper insight into the origin of excitonic peaks that contribute to the $\epsilon_2(\omega)$, we have plotted the oscillator strength of excitons for both silicides in Figs. 3(c) and 3(d). If it is negligibly small, exciton is known to be dark; otherwise it is considered bright for its contribution to the spectrum. The strength of the excitons in Mg_2Si is comparably larger than those for Ca_2Si . The first bright exciton in Fig. 3(c) is estimated

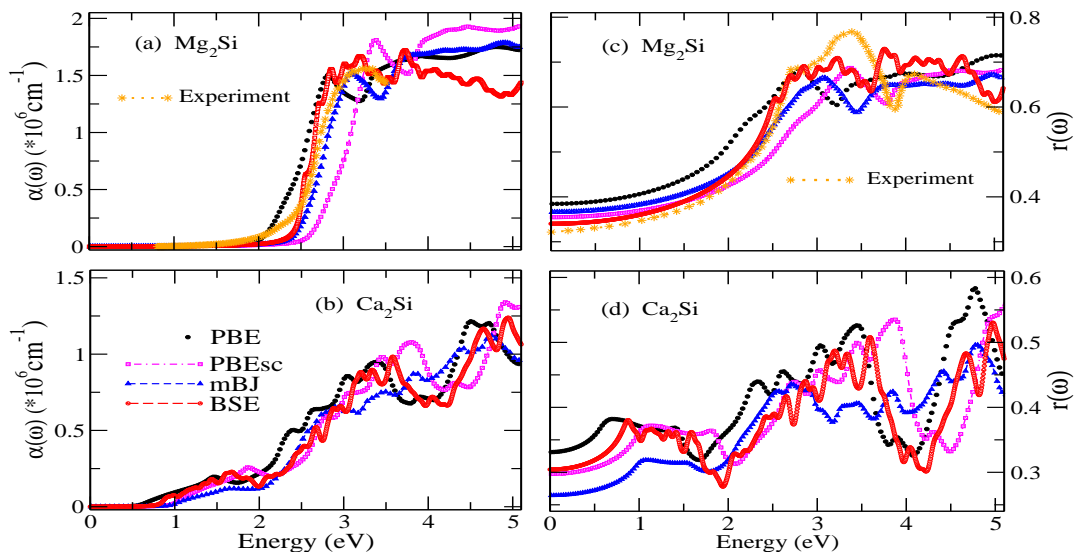


FIG. 5: Calculated absorption coefficient $\alpha(\omega)$ and reflectivity $r(\omega)$ for Mg_2Si and Ca_2Si : a comparison of IPA methods (PBE, PBE+scissor (PBEsc), and mBJ) with the Bethe-Salpeter equation (BSE). The experimental data in panels (a) and (c) are from references [35] and [33], respectively.

at ~ 2.54 eV with an intensity of ~ 0.041 , making a contribution to the formation of a little hump in the Mg_2Si $\epsilon_2(\omega)$ spectrum. The second significant bright exciton, seen at ~ 2.7 eV, originates the highest peak comparable to the experiment in the BSE spectrum. For Ca_2Si , the only bound bright exciton in Fig. 3(d) appears at ~ 0.89 eV, which is below the direct gap of ~ 0.96 eV. Its binding energy of only 70 meV indicates that this exciton is loosely bound. This may be attributed to the lower band gap as well as lower m_{dos}^* value of electron at ϵ_c [58, 77] (see Table II) in Ca_2Si . So, this bound exciton can easily dissociate into free carriers with the aid of heat energy or additional photons. This can enhance charge carrier generation in Ca_2Si , making it more efficient for applications like solar cells. After an optical energy region, both silicides have a large number of dark excitons and may have an insignificant contribution of effective two QP excitons at static screening to the $\epsilon_2(\omega)$ in quantitative agreement with experiment.

Fig. 4 illustrates the computed real $n(\omega)$ and imaginary $k(\omega)$ parts of the refractive index for both silicides using IPA and BSE. The $n(\omega)$ ($k(\omega)$) follows the same trend as observed in the $\epsilon_1(\omega)$ ($\epsilon_2(\omega)$) plot for the respective compounds. The range of $n(0)$ is observed to be ~ 3.8 – 4.26 for Mg_2Si and 3.1 – 3.7 for Ca_2Si . This can be attributed to the inverse relationship between refractive index and band gap, since the band gap of the former is lower than that of the latter (see Table I) [78]. The $n(0)$ value from BSE of ~ 3.8 is found to be very close to the experimental $n(0)$ of ~ 3.6 [33] for Mg_2Si . Also, the maximum $n(\omega)$ using BSE of ~ 7.9 at ~ 2.5 eV is fairly good agreement with the experimental magnitude of ~ 7.7 at ~ 2.55 eV. Next, the range of maximum intensity of $k(\omega)$ for Mg_2Si and Ca_2Si is found to be ~ 2.6 – 4.0

eV and ~ 2.4 – 4.0 eV, respectively. This implies that in this energy range, photons will be absorbed very quickly (i.e., the penetration depth will be the shortest within this range). The highest $k(\omega)$ of ~ 5.4 at ~ 2.85 eV photon energy from BSE has the best matching with experimental peak of 5.4 at ~ 2.95 eV [33]. Overall, both $n(\omega)$ and $k(\omega)$ have larger values for Mg_2Si than Ca_2Si in the studied energy range. Due to the large $n(\omega)$ ($\sim >3$) of both silicides, they can be the best materials to design the anti-reflection coating surface on solar devices [79].

We compare in Fig. 5 the absorption coefficient $\alpha(\omega)$ and reflectivity $r(\omega)$ from IPA with BSE calculations. The $\alpha(\omega)$ from spectroscopic ellipsometry measurement by *Kato et al.* [35] on poly-crystalline Mg_2Si thin-film is also plotted for comparison in Fig. 5(a). In this figure, the red-shift of the PBE $\alpha(\omega)$ has become the blue-shift after applying the scissor correction on PBE (PBEsc) with respect to the experiment. Additionally, the presence of e - h interaction on PBEsc significantly improves the $\alpha(\omega)$ and aligns well with the experiment. Beyond the optical gap edge (~ 2.45 eV), the agreement of $\alpha(\omega)$ (from BSE) with the experiment is satisfactory, and below the gap it is not matching due to consideration of direct optical transitions only. One can also notice that the BSE $\alpha(\omega)$ increases rapidly from an optical gap onset to an edge of the visible energy region of ~ 3.2 eV and then decreases as oscillatory type in the UV energy region. In Fig. 5(b), the $\alpha(\omega)$ from all IPA and BSE methods has been increased monotonically with photon energy. Also, we do not observe a significant change, especially up to visible light, in the BSE spectrum compared to the QP-corrected PBEsc spectrum, which means two interacting QP picture may be less effective in Ca_2Si . The highest intense peak in the visible energy regime (at

~ 3.2 eV) is found to be ~ 1.7 and $\sim 0.9 \times 10^6$ cm^{-1} for Mg_2Si and Ca_2Si , respectively. Further, for Mg_2Si , the BSE calculation has provided a comparable $r(\omega)$ up to visible energy region to the Scouler reflectance measurement [33] in Fig. 5(c). In the considered UV light region, the $r(\omega)$ underestimates (overestimates) experimental data for photon energies below (above) ~ 3.7 eV. The minimum $r(\omega)$ for visible light from BSE is estimated to be $\sim 41\%$. The spectrum from all methods initially shows a linear increase in behaviour (same as experiment) up to their highest value in the visible energy region, and after that, the spectrum does not show too many changes with energy. In Fig. 5(d), the $r(\omega)$ in Ca_2Si exhibits a more of an oscillatory nature within the studied energy window across all methods. In the infrared (IR) region, the mBJ method provides the lowest $r(\omega)$ among all the methods. Beyond this region, the spectrum with excitonic contributions in PBesc (BSE) yield the lowest values, particularly in the visible light, reaching a minimum of $\sim 27\%$. This low reflectivity suggests that Ca_2Si could be used to make an anti-reflective coating surface.

The optical properties obtained for Mg_2Si are much more comparable to those of silicon, while the properties for Ca_2Si show a better match with various solar compounds such as InAs, GaAs, and GaP [80]. However, possessing excellent optical properties is not a sufficient criterion for using materials in PV technology. Therefore, it is essential to examine the material's power conversion efficiency to determine its suitability for solar cells.

C. SLME and defect-aided SRH mechanisms

The light to electricity conversion efficiency from solar cells depends on the extraction of e - h pairs by materials and is limited by the various e - h recombination processes. In this paper, SLME of single-junctional PV cell is calculated from current-voltage analysis, explicitly focusing on radiative recombination [15]. While, the trap-limited conversion (TLC) efficiency η_{TLC} is estimated by considering both radiative and non-radiative recombination mechanisms [17, 21, 23]. We mainly consider the optoelectronic and point-defect properties of materials. Let us first discuss the radiative limit. Following the Shockley diode equation, the radiative recombination current density J_{rad} for net voltage across the cell (V) can be estimated by [17],

$$J_{rad} = J_{rad}^0 \left(e^{(eV/k_B T)} - 1 \right), \quad (6)$$

and J_{rad}^0 is due to black-body photons at temperature T absorbed by the front cell surface from the surrounding thermal bath

$$J_{rad}^0 = e\pi \int_0^\infty \left(1 - e^{-2\alpha(\varepsilon)L} \right) I_{bb}(\varepsilon, T) d\varepsilon, \quad (7)$$

with $I_{bb}(\varepsilon, T)$ is the black-body radiance related to the radiative process, e is the elementary charge and k_B is

the Boltzmann constant. $\alpha(\varepsilon)$ is material absorption coefficient and L is the thickness of an absorber layer with zero and unity-reflectivity from the front and back surface (hence the presence of factor 2), respectively.

In the case of non-radiative recombination, e - h pairs recombine through trap states within the band gap, as described by the SRH model [26]. In the high-injection limit where both charge carriers are present in almost similar concentration, the non-radiative current density is [17];

$$\begin{aligned} J_{nr} &= J_{nr}^0 \left(e^{(eV/2k_B T)} - 1 \right), \\ J_{nr}^0 &= \frac{eL\sqrt{N_c N_v}}{2\tau} e^{-\varepsilon_g/2k_B T}, \\ N_c &= \int_{\varepsilon_c}^\infty g_c(\varepsilon) e^{-\frac{(\varepsilon-\varepsilon_c)}{k_B T}} d\varepsilon, \quad N_v = \int_{-\infty}^{\varepsilon_v} g_v(\varepsilon) e^{-\frac{(\varepsilon_v-\varepsilon)}{k_B T}} d\varepsilon. \end{aligned} \quad (8)$$

where N_c (N_v) and $g_c(\varepsilon)$ ($g_v(\varepsilon)$) are an effective and total density of states in the CB (VB), respectively [58]. ε_g is the band gap of an absorber and τ is the nonradiative recombination lifetime (or SRH lifetime).

Finally the trap-limited current density J of an illuminating solar cell under photon flux at bias voltage V is given by,

$$J(V; L) = J_{sc}(L) - J_{rad}(V; L) - J_{nr}(V; L). \quad (9)$$

The first term is the short-circuit current density and defined as,

$$J_{sc} = e \int_0^\infty \left(1 - e^{-2\alpha(\varepsilon)L} \right) I_{sun}(\varepsilon) d\varepsilon, \quad (10)$$

where $I_{sun}(\varepsilon)$ is the incident total number of photons of energy ε per unit area, energy and time, and standard AM1.5G flat-plate solar spectrum at 25 °C [81] is used for this. Finally, the η_{TLC} from maximum output power is defined as,

$$\eta_{TLC} = \frac{\max(J \times V)}{\int_0^\infty \varepsilon I_{sun}(\varepsilon) d\varepsilon}. \quad (11)$$

In SLME formalism [15, 70], for calculating J , only first two terms in right side of Eq. (9) are considered. The extra factor $e^{\Delta/k_B T}$, which is the fraction of the radiative recombination current, is also multiplied in Eq. (6). The $\Delta = \varepsilon_g^{da} - \varepsilon_g$, where ε_g^{da} is direct-allowed band gap of material. Then the estimated J is used in Eq. (11) to calculate SLME.

Next, the TLC efficiency of PV solar cell can be calculated by solving Eq. (11) after information on electronic dispersion, carrier recombination lifetime τ , absorption coefficient, and the thickness L of an absorbing layer. Now let us develop an expression of τ . As we have already discussed in the introduction that, the SRH model defines the recombination rate of e - h pairs via a trapping state inside the band gap [26]. Based on the principle of detailed balance, the SRH recombination rate

(R_{SRH}) of electrons in ε_c and holes in ε_v associated to a defect density N_d of a single trap state t at an energy ε_t is given by [26, 27],

$$R_{SRH} = \frac{np - n_0p_0}{\tau_{n0}(n + n_t) + \tau_{p0}(p + p_t)}, \quad (12)$$

where,

$$\tau_{n0} = \frac{1}{N_d C_n}, \quad \tau_{p0} = \frac{1}{N_d C_p}, \quad (13)$$

$$n_t = N_c e^{-(\varepsilon_c - \varepsilon_t)/k_B T}, \quad p_t = N_v e^{-(\varepsilon_t - \varepsilon_v)/k_B T}.$$

Here τ_{n0} , C_n and τ_{p0} , C_p are the capture time constants, capture coefficients for an electron in CB and a hole in VB at trap state t , respectively. After that, n_t and p_t are the number of electrons and holes for the case in which ε_F falls at ε_t .

Accordingly, the steady-state density of electrons n and holes p under applied voltage V (or under illumination) for Eq. (12) can be estimated by:

$$n = n_0 + \Delta n, \quad \text{and} \quad p = p_0 + \Delta n. \quad (14)$$

Finally, the carrier lifetime associated to the recombination rate R_{SRH} with excess carrier densities Δn generated from illumination is given by,

$$\tau = \frac{\Delta n}{R_{SRH}}. \quad (15)$$

Now, the unknown quantities to calculate τ in Eq. (15) are basically concentrations (n_0 , p_0 , Δn , and N_d), ε_t and $C_{n/p}$, which can be estimated from the point defect calculations. The main quantity, which is needed to define the point defect in a system is its formation energy. From the supercell approach, the formation energy $\Delta E_f(d^q)$ of any point defect d in charge state q can be written as follows [82];

$$\Delta E_f(d^q) = G(d) - G(\text{bulk}) - \sum_i n_i \mu_i + q(\varepsilon_v + \varepsilon_F). \quad (16)$$

where $G(d)$ and $G(\text{bulk})$ are the free energies of defect containing and pristine supercells, respectively. The integer n_i defines the number of i type atoms which have been added to ($n_i > 0$) or removed from ($n_i < 0$) the pristine supercell to make a defective system, and μ_i are the respective chemical potentials of the defect species.

We shall now calculate the equilibrium concentrations of a defect and carriers. Typically, we need to know the ε_F to obtain these concentrations. For this purpose, we have used a Fortran code named SC-FERMI [83], which employs an iterative search algorithm to calculate the ε_F that satisfies the charge neutrality constraint for the overall system. This value of ε_F is termed the ‘‘self-consistent Fermi energy’’, and used to calculate $\Delta E_f(d^q)$ in Eq. (16). Then the intrinsic electron, hole (n_0 , p_0) concentrations without illuminating light, as well as the

equilibrium concentration of a defect $N_d(q)$ for q , are calculated as follows [58, 83]:

$$n_0 = N_c e^{-(\varepsilon_c - \varepsilon_F)/k_B T}, \quad p_0 = N_v e^{-(\varepsilon_F - \varepsilon_v)/k_B T}, \quad (17)$$

$$N_d(q) = N_{\text{site}} g e^{-\Delta E_f(d^q)/k_B T}.$$

where, N_{site} and g represent the density of available crystal sites and the degeneracy for defect d , respectively. For simplicity, we set g to 1.

Based on charge neutrality condition for defects and carriers, one can write [58, 83],

$$\sum_{q,d} q N_d(q) = p_0 - n_0. \quad (18)$$

The dependence of each term in Eq. (18) on ε_F allows for the use of a search algorithm to iteratively update ε_F until it satisfies the requirements of Eq. (18) at a given temperature.

The defect formation energies (DFE) of both compounds for two point vacancy defects ($V_{Mg/Ca}$ and V_{Si}), two interstitial defects ($I_{Mg/Ca}$ and I_{Si}), and anti-site defects (Mg/Ca_{Si} and $Si_{Mg/Ca}$) have been calculated at $q = 0$ and tabulated in Table III. The DFE of these native defects are obtained in growth conditions rich in Si , where $\mu_{Si} = E(Si)$, and $\mu_{Mg} = (1/2)(E(Mg_2Si) - E(Si))$. The $E(Mg_2Si)$ and $E(Si)$ are energies of a bulk stable Mg_2Si and Si in FCC structures, respectively. The order of calculated DFE from Table III is: $I_{Mg} < Mg_{Si} < V_{Mg} < V_{Si} < I_{Si} < V_{MgSi} < Si_{Mg}$ for Mg_2Si and $I_{Si} < Si_{Ca} < I_{Ca} < Ca_{Si} < V_{Si} < V_{Ca} < V_{CaSi}$ for Ca_2Si . Due to low DFE, the interstitial Mg (I_{Mg}) and Si (I_{Si}) atoms on $4b$ sites are the most favorable/stable defects compared to other defects in Mg_2Si and Ca_2Si , respectively. The next most stable defects is due to anti-site with Mg_{Si} and Si_{Ca} in the both respective silicides. Thus, we will further calculate R_{SRH} and τ by considering only a single local single-particle defect state, which is due to I_{Mg} (I_{Si}) interstitial defect in the pristine structure of Mg_2Si (Ca_2Si).

TABLE III: The obtained defect formation energies (DFE) from PBE for different types of point defects on Mg_2Si and Ca_2Si in Si-rich condition.

Defects in Mg_2Si	DFE (eV/atom)	Defects in Ca_2Si	DFE (eV/atom)
V_{Mg}	1.50	V_{Ca}	2.37
V_{Si}	2.23	V_{Si}	2.00
Mg_{Si}	1.47	Ca_{Si}	1.91
Si_{Mg}	2.90	Si_{Ca}	1.53
I_{Si}	2.44	I_{Si}	1.24
I_{Mg}	1.35	I_{Ca}	1.65
V_{MgSi}	2.66	V_{CaSi}	3.12

The carrier capture coefficient ($C_{n/p}$) is related to the capture cross section σ and the thermal velocity

TABLE IV: Photovoltaic performance parameters of Mg_2Si and Ca_2Si using the Bethe-Salpeter equation (BSE) based absorption coefficient at 300 K, predicted by spectroscopic limited maximum efficiency (SLME), Shockley–Queisser (SQ) limit, and trap-limited conversion efficiency (η_{TLC}). J_{sc} is the short-circuit current density and V_{oc} is the open-circuit voltage.

Solar materials	SRH lifetime	$J_{sc}(mAcm^{-2})$	$V_{oc}(V)$	η_{TLC}	SLME	SQ-limit
Mg_2Si	$2 \mu s$	6.8	0.55	1.2%	1.3%	19.37%
Ca_2Si	$11.3 ms$	50.5	0.7	28.5%	31.2%	31.25%

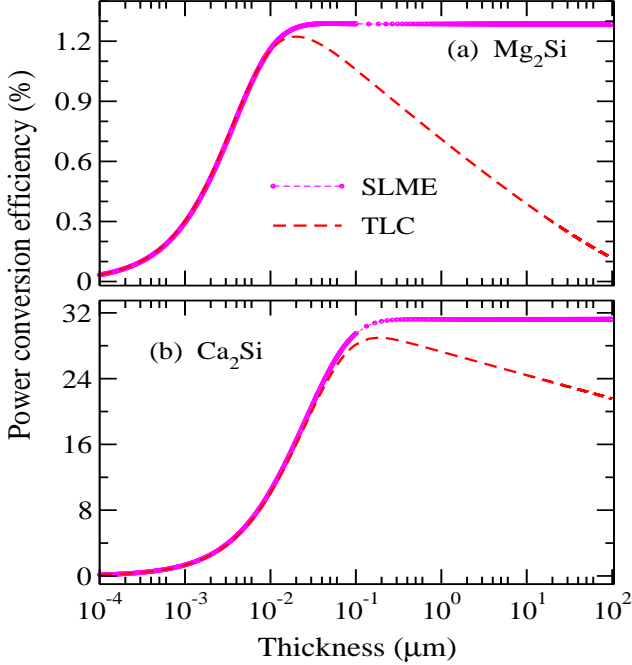


FIG. 6: Spectroscopic limited maximum efficiency (SLME) and trap-limited conversion (TLC) efficiency using absorption coefficient from Bethe-Salpeter equation (BSE) method for (a) Mg_2Si (b) Ca_2Si as a function of thickness.

ν via $C = \sigma\nu$. The *ab-initio* computation of σ is very expensive, thus we assume the same σ for both charge carriers ($10^{-15}cm^2$) in both materials, a typical value used for deep defect states [24, 82]. The thermal velocity ν at particular temperature for electrons and holes is directly estimated from the carrier effective masses [22]. Moreover, the carrier densities (Δn) under illumination of light are kept fixed to $10^{15}cm^{-3}$ in both silicides, a typical value used in many PV materials such as CdTe [84] and kesterite $\text{Cu}_2\text{ZnSnS}_4$ (CZTS) [85]. The ϵ_t levels above the ϵ_v for most stable defects in Mg_2Si and Ca_2Si are found to be ~ 0.4 and 0.6 eV, respectively. Based on this information, in Table IV, the SRH lifetime (τ) is calculated to be $\sim 2 \mu s$ for Mg_2Si , which is comparable to the lifetimes observed in various Cu-based solar ma-

terials [86]. For Ca_2Si , the SRH lifetime is $\sim 11.3 ms$, slightly higher than the $8.8 ms$ lifetime for silicon [87]. Now, the SLME and η_{TLC} at 300 K for both silicides, obtained using the BSE absorption spectrum, are presented in Fig. 6. The figure indicates that both values remain nearly the same up to a certain thickness. However, beyond this thickness, the TLC value drops below that of the SLME up to the studied thickness. This behavior, as understood from Eq. (8), can be attributed to significantly lower non-radiative recombination losses in thinner layers compared to thicker ones for both materials. Additionally, it is noted that the rate of decrease in TLC efficiency for Mg_2Si is greater than that for Ca_2Si , possibly due to a comparatively much lower τ for Mg_2Si than for Ca_2Si . In Table IV, the highest SLME for Mg_2Si is $\sim 1.3\%$, which is very low compared to the SQ-limit of $\sim 19.37\%$. When considering non-radiative recombination, the highest η_{TLC} is $\sim 1.2\%$, showing no significant change compared to the SLME. One possible explanation for lower values is the large direct band gap (~ 2.45 eV), which results in a reduced contribution from the visible energy portion in the η_{TLC} computation. This leads to a very low J_{sc} value of $\sim 6.8 mAcm^{-2}$, resulting in a minimal output power. In Table IV, the maximum η_{TLC} of $\sim 28.5\%$ is lower than, as expected, the highest SLME of $\sim 31.2\%$ for Ca_2Si , and both values are below the SQ-limit of $\sim 31.25\%$. The inclusion of non-radiative recombination losses reduces the highest efficiency value by only 2.7% compared to the radiative limit (SLME). This TLC efficiency is comparable to that of silicon-based solar cells (26.7%) [87]. Additionally, it is higher than the efficiencies of other materials, including CdTe (21%), Cu(In,Ga)(S,Se)₂ (CIGS) at 21.7%, halide perovskite (20.9%) [87], and various kesterite solar materials (21-24%) [23].

Based on these results, one can conclude that Ca_2Si can be effectively used to develop single-junction thin-film solar devices. In contrast, the significantly lower TLC efficiency of Mg_2Si makes it less suitable for single-junction applications. However, it may be effective as a bottom cell to absorb the lower-energy portion of the solar spectrum in multi-junction PV modules. It is worth noting that the obtained η_{TLC} is associated with only one local single-defect level in the band gap. However, in reality, multiple local single-particle defect states can exist

for a defect from various mid-gap transition levels [88]. The presence of these multiple trap levels significantly reduces R_{SRH} , as defects often become trapped in their highest or lowest charge states. Conversely, the inclusion of excited states can enhance the R_{SRH} by several orders of magnitude, effectively balancing the former reduction [88]. Consequently, the overall calculated η_{TLC} may not significantly change when accounting both factors in calculations. While accounting for recombination losses at the material interface [22] could influence the calculated η_{TLC} , such investigations are beyond the scope of this paper. Future studies could explore the impact of these multilevel and surface recombination loss mechanisms on TLC efficiency.

IV. CONCLUSIONS

In summary, we systematically investigate the electronic and optical properties of cheap, eco-friendly, and earth-abundant Mg_2Si and Ca_2Si materials using *first principles* based DFT and BSE methods, while also evaluating their solar performance factors. The calculated indirect and direct band-gaps are in the range of 0.25-0.6 eV and 0.57-0.96 eV for Mg_2Si and Ca_2Si , respectively. We also obtain the m_d^* of electrons and holes

at high-symmetric points for band extrema. In IPA, the $\epsilon_1(\omega)$ and $\epsilon_2(\omega)$ exhibit peak values of ~ 50 (2.6 eV) and ~ 61 (3.24 eV) for Mg_2Si , while for Ca_2Si , the values are ~ 16.3 (1 eV) and ~ 16.2 (3.4 eV), respectively. Inclusion of the excitonic effect in BSE solution raises the highest IPA peak of $\epsilon_1(\omega)$ ($\epsilon_2(\omega)$) to ~ 59 (65) for Mg_2Si , and ~ 17 (16.6) for Ca_2Si , with a shift towards lower energy. Both silicides demonstrate a large $\alpha(\omega)$ (order of 10^6 cm^{-1}) and $r(\omega)$ of less than 40% in the active region of solar spectrum. The study illustrates the effectiveness of employing various theoretical methodology to accurately describe the properties of silicides.

On the other hand, we have examined the performance of silicides by calculating efficiency based on (i) explicitly considering only radiative recombination using the SLME formalism and (ii) both radiative and non-radiative $e-h$ recombination using the TLC model. We find the interstitial Mg (Si) defect in Mg_2Si (Ca_2Si) to be more energetically favorable than other studied point defects. At 300 K, the highest SLME value is obtained to be ~ 1.3 (31.2)% for Mg_2Si (Ca_2Si), which is further reduced to be ~ 1.2 (28.5)% in the TLC calculation. The findings serve as useful guidelines for the experimental community in designing silicide-based solar devices and understanding their PV mechanisms.

-
- [1] J. M. Rondinelli and E. Kioupakis, Predicting and designing optical properties of inorganic materials, *Annu. Rev. Mater. Res.* **45**, 491 (2015).
- [2] M. L. Cohen and J. R. Chelikowsky, *Electronic Structure and Optical Properties of Semiconductors*, Vol. 75 (Springer Berlin Heidelberg, 1988).
- [3] Z. H. Levine and D. C. Allan, Linear optical response in silicon and germanium including self-energy effects, *Phys. Rev. Lett.* **63**, 1719 (1989).
- [4] G. Onida, L. Reining, and A. Rubio, Electronic excitations: density-functional versus many-body Green's-function approaches, *Rev. Mod. Phys.* **74**, 601 (2002).
- [5] F. Bechstedt, *Many-body approach to electronic excitations* (Springer Berlin, Heidelberg, 2016).
- [6] M. Rohlfing and S. G. Louie, Electron-hole excitations and optical spectra from first principles, *Phys. Rev. B* **62**, 4927 (2000).
- [7] V. Begum, M. E. Gruner, C. Vorwerk, C. Draxl, and R. Pentcheva, Theoretical description of optical and x-ray absorption spectra of MgO including many-body effects, *Phys. Rev. B* **103**, 195128 (2021).
- [8] A. G. Marinopoulos and M. Grüning, Local-field and excitonic effects in the optical response of α -alumina, *Phys. Rev. B* **83**, 195129 (2011).
- [9] L. X. Benedict, E. L. Shirley, and R. B. Bohn, Optical absorption of insulators and the electron-hole interaction: An ab initio calculation, *Phys. Rev. Lett.* **80**, 4514 (1998).
- [10] E. K. Chang, M. Rohlfing, and S. G. Louie, Excitons and optical properties of α -quartz, *Phys. Rev. Lett.* **85**, 2613 (2000).
- [11] B. Arnaud and M. Alouani, Local-field and excitonic effects in the calculated optical properties of semiconductors from first-principles, *Phys. Rev. B* **63**, 085208 (2001).
- [12] E. E. Salpeter and H. A. Bethe, A relativistic equation for bound-state problems, *Phys. Rev.* **84**, 1232 (1951).
- [13] S. Albrecht, L. Reining, R. Del Sole, and G. Onida, Ab initio calculation of excitonic effects in the optical spectra of semiconductors, *Phys. Rev. Lett.* **80**, 4510 (1998).
- [14] C. Vorwerk, B. Aurich, C. Cocchi, and C. Draxl, Bethe-Salpeter equation for absorption and scattering spectroscopy: implementation in the exciting code, *Electron. Struct.* **1**, 037001 (2019).
- [15] L. Yu and A. Zunger, Identification of potential photovoltaic absorbers based on first-principles spectroscopic screening of materials, *Phys. Rev. Lett.* **108**, 068701 (2012).
- [16] V. L. Dalal and A. R. Moore, Design considerations for high-intensity solar cells, *J. Appl. Phys.* **48**, 1244 (1977).
- [17] T. Kirchartz and U. Rau, What makes a good solar cell?, *Adv. Energy Mater.* **8**, 1703385 (2018).
- [18] I.-H. Lee, J. Lee, Y. J. Oh, S. Kim, and K. J. Chang, Computational search for direct band gap silicon crystals, *Phys. Rev. B* **90**, 115209 (2014).
- [19] W.-J. Yin, T. Shi, and Y. Yan, Unique properties of halide perovskites as possible origins of the superior solar cell performance, *Adv. Mater.* **26**, 4653 (2014).
- [20] W. Shockley and H. J. Queisser, Detailed Balance Limit of Efficiency of p-n Junction Solar Cells, *J. Appl. Phys.* **32**, 510 (1961).
- [21] J. Nelson, *The Physics of Solar Cells* (Imperial College,

- London, 2003).
- [22] A. Smets, K. Jäger, O. Isabella, R. Van Swaaij, and M. Zeman, *Solar Energy: The Physics and Engineering of Photovoltaic Conversion, Band Structures, and System Applications* (Bloomsbury USA, 2016).
- [23] S. Kim, J. A. Márquez, T. Unold, and A. Walsh, Upper limit to the photovoltaic efficiency of imperfect crystals from first principles, *Energy Environ. Sci.* **13**, 1481 (2020).
- [24] L. Shi and L.-W. Wang, Ab initio calculations of deep-level carrier nonradiative recombination rates in bulk semiconductors, *Phys. Rev. Lett.* **109**, 245501 (2012).
- [25] Y. Xu, J.-H. Yang, S. Chen, and X.-G. Gong, Defect-assisted nonradiative recombination in $Cu_2ZnSnSe_4$: A comparative study with Cu_2ZnSnS_4 , *Phys. Rev. Mater.* **5**, 025403 (2021).
- [26] W. Shockley and W. T. Read, Statistics of the recombinations of holes and electrons, *Phys. Rev.* **87**, 835 (1952).
- [27] R. N. Hall, Electron-hole recombination in germanium, *Phys. Rev.* **87**, 387 (1952).
- [28] F. D'heurle and L. Miglio, *Silicides: Fundamentals & Applications* (World Scientific, Singapore, 2000).
- [29] V. E. Borisenko, *Semiconducting Silicides* (Springer Berlin, Heidelberg, 2013).
- [30] Z. Liu, S. Wang, N. Ootogawa, Y. Suzuki, M. Osamura, Y. Fukuzawa, T. Ootsuka, Y. Nakayama, H. Tanoue, and Y. Makita, A thin-film solar cell of high-quality $\beta - FeSi_2/Si$ heterojunction prepared by sputtering, *Sol. Energy Mater. Sol. Cells* **90**, 276 (2006).
- [31] Y. Makita, T. Ootsuka, Y. Fukuzawa, N. Ootogawa, H. Abe, Z. Liu, and Y. Nakayama, $\beta - FeSi_2$ as a kankyo (environmentally friendly) semiconductor for solar cells in the space application, in *Photonics for Solar Energy Systems*, Vol. 6197, International Society for Optics and Photonics (SPIE, 2006) p. 61970O.
- [32] H. Udono, H. Tajima, M. Uchikoshi, and M. Itakura, Crystal growth and characterization of Mg_2Si for IR-detectors and thermoelectric applications, *Jpn. J. Appl. Phys.* **54**, 07JB06 (2015).
- [33] W. J. Scouler, Optical properties of Mg_2Si , Mg_2Ge , and Mg_2Sn from 0.6 to 11.0 eV at 77 K, *Phys. Rev.* **178**, 1353 (1969).
- [34] R. G. Morris, R. D. Redin, and G. C. Danielson, Semiconducting properties of Mg_2Si single crystals, *Phys. Rev.* **109**, 1909 (1958).
- [35] T. Kato, Y. Sago, and H. Fujiwara, Optoelectronic properties of Mg_2Si semiconducting layers with high absorption coefficients, *J. Appl. Phys.* **110**, 063723 (2011).
- [36] J. E. Mahan, A. Vantomme, G. Langouche, and J. P. Becker, Semiconducting Mg_2Si thin films prepared by molecular-beam epitaxy, *Phys. Rev. B* **54**, 16965 (1996).
- [37] D. Tamura, R. Nagai, K. Sugimoto, H. Udono, I. Kikuma, H. Tajima, and I. J. Ohsugi, Melt growth and characterization of Mg_2Si bulk crystals, *Thin Solid Films* **515**, 8272 (2007).
- [38] M. W. Heller and G. C. Danielson, Seebeck effect in Mg_2Si single crystals, *J. Phys. Chem. Solids* **23**, 601 (1962).
- [39] J. L. Corkill and M. L. Cohen, Structural, bonding, and electronic properties of IIA-IV antiferroite compounds, *Phys. Rev. B* **48**, 17138 (1993).
- [40] Y. Imai, A. Watanabe, and M. Mukaida, Electronic structures of semiconducting alkaline-earth metal silicides, *J. Alloys Compd.* **358**, 257 (2003).
- [41] F. Aymerich and G. Mula, Pseudopotential band structures of systems Mg_2Si , Mg_2Ge , Mg_2Sn , and of the solid solution $Mg_2(Ge, Sn)$, *Phys. status solidi (b)* **42**, 697 (1970).
- [42] M. Y. Au-Yang and M. L. Cohen, Electronic structure and optical properties of Mg_2Si , Mg_2Ge , and Mg_2Sn , *Phys. Rev.* **178**, 1358 (1969).
- [43] V. V. Sobolev, Reflectivity spectra and energy band structure of Mg_2X crystals, *Phys. Status Solidi (b)* **49**, K209 (1972).
- [44] D. McWilliams and D. W. Lynch, Infrared reflectivities of magnesium silicide, germanide, and stannide, *Phys. Rev.* **130**, 2248 (1963).
- [45] F. Vazquez, R. A. Forman, and M. Cardona, Electroreflectance measurements on Mg_2Si , Mg_2Ge , and Mg_2Sn , *Phys. Rev.* **176**, 905 (1968).
- [46] D. B. Migas, L. Miglio, V. L. Shaposhnikov, and V. E. Borisenko, Comparative study of structural, electronic and optical properties of Ca_2Si , Ca_2Ge , Ca_2Sn , and Ca_2Pb , *Phys. Rev. B* **67**, 205203 (2003).
- [47] S. Lebègue, B. Arnaud, and M. Alouani, Calculated quasiparticle and optical properties of orthorhombic and cubic Ca_2Si , *Phys. Rev. B* **72**, 085103 (2005).
- [48] P. Blaha, K. Schwarz, F. Tran, R. Laskowski, G. K. H. Madsen, and L. D. Marks, WIEN2k: An APW+lo program for calculating the properties of solids, *J. Chem. Phys.* **152**, 074101 (2020).
- [49] J. P. Perdew, K. Burke, and M. Ernzerhof, Generalized gradient approximation made simple, *Phys. Rev. Lett.* **77**, 3865 (1996).
- [50] J. P. Perdew, A. Ruzsinszky, G. I. Csonka, O. A. Vydrov, G. E. Scuseria, L. A. Constantin, X. Zhou, and K. Burke, Restoring the density-gradient expansion for exchange in solids and surfaces, *Phys. Rev. Lett.* **100**, 136406 (2008).
- [51] F. Tran and P. Blaha, Accurate band gaps of semiconductors and insulators with a semilocal exchange-correlation potential, *Phys. Rev. Lett.* **102**, 226401 (2009).
- [52] O. Rubel, F. Tran, X. Rocquefelte, and P. Blaha, Perturbation approach to ab initio effective mass calculations, *Comput. Phys. Commun.* **261**, 107648 (2021).
- [53] J. J. Pulikkotil, D. J. Singh, S. Auluck, M. Saravanan, D. K. Misra, A. Dhar, and R. C. Budhani, Doping and temperature dependence of thermoelectric properties in $Mg_2(Si, Sn)$, *Phys. Rev. B* **86**, 155204 (2012).
- [54] S. Curtarolo, W. Setyawan, G. L. Hart, M. Jahnatek, R. V. Chepulskii, R. H. Taylor, S. Wang, J. Xue, K. Yang, O. Levy, M. J. Mehl, H. T. Stokes, D. O. Demchenko, and D. Morgan, AFLOW: An automatic framework for high-throughput materials discovery, *Comput. Mater. Sci.* **58**, 218 (2012).
- [55] J. P. Perdew and M. Levy, Physical content of the exact Kohn-Sham orbital energies: Band gaps and derivative discontinuities, *Phys. Rev. Lett.* **51**, 1884 (1983).
- [56] Y.-S. Kim, M. Marsman, G. Kresse, F. Tran, and P. Blaha, Towards efficient band structure and effective mass calculations for III-V direct band-gap semiconductors, *Phys. Rev. B* **82**, 205212 (2010).
- [57] D. Koller, F. Tran, and P. Blaha, Merits and limits of the modified Becke-Johnson exchange potential, *Phys. Rev. B* **83**, 195134 (2011).
- [58] N. W. Ashcroft and N. D. Mermin, *Solid State Physics*

- (Holt, Rinehart and Winston, New York, 1976).
- [59] W. G. Spitzer and H. Y. Fan, Determination of optical constants and carrier effective mass of semiconductors, *Phys. Rev.* **106**, 882 (1957).
- [60] S. O. Kasap, *Principles of electronic materials and devices* (New York:McGraw-Hill, 2006).
- [61] M. A. Green, Intrinsic concentration, effective densities of states, and effective mass in silicon, *J. Appl. Phys.* **67**, 2944 (1990).
- [62] P. M. Lee, Electronic structure of magnesium silicide and magnesium germanide, *Phys. Rev.* **135**, A1110 (1964).
- [63] W. Schäfer and M. Wegener, *Semiconductor Optics and Transport Phenomena* (Springer Berlin, Heidelberg, 2013).
- [64] G. S. Nolas, D. Wang, and M. Beekman, Transport properties of polycrystalline $Mg_2Si_{1-y}Sb_y$ ($0 \leq y < 0.4$), *Phys. Rev. B* **76**, 235204 (2007).
- [65] M. R. Ashwin Kishore and P. Ravindran, Tailoring the electronic band gap and band edge positions in the C_2N monolayer by P and As substitution for photocatalytic water splitting, *J. Phys. Chem. C* **121**, 22216 (2017).
- [66] T. Le Bahers, M. Rerat, and P. Sautet, Semiconductors used in photovoltaic and photocatalytic devices: assessing fundamental properties from dft, *J. Phys. Chem. C* **118**, 5997 (2014).
- [67] N. V. Smith, Photoelectron energy spectra and the band structures of the noble metals, *Phys. Rev. B* **3**, 1862 (1971).
- [68] C. Ambrosch-Draxl and J. O. Sofo, Linear optical properties of solids within the full-potential linearized augmented planewave method, *Comput. Phys. Commun.* **175**, 1 (2006).
- [69] S. Sagmeister and C. Ambrosch-Draxl, Time-dependent density functional theory versus Bethe-Salpeter equation: an all-electron study, *Phys. Chem. Chem. Phys.* **11**, 4451 (2009).
- [70] V. K. Solet, S. Sk, and S. K. Pandey, First-principles study of optoelectronic and thermoelectronic properties of the $ScAgC$ half-Heusler compound, *Phys. Scr.* **97**, 105711 (2022).
- [71] S. Sk, P. Devi, S. Singh, and S. K. Pandey, Exploring the best scenario for understanding the high temperature thermoelectric behaviour of Fe_2VAl , *Mater. Res. Express* **6**, 026302 (2018).
- [72] S. S. Shastri and S. K. Pandey, First-principles electronic structure, phonon properties, lattice thermal conductivity and prediction of figure of merit of $FeVSb$ half-Heusler, *J. Phys.: Condens. Matter.* **33**, 085704 (2020).
- [73] S. S. Shastri and S. K. Pandey, Thermoelectric properties, efficiency and thermal expansion of $ZrNiSn$ half-Heusler by first-principles calculations, *J. Phys.: Condens. Matter.* **32**, 355705 (2020).
- [74] L. Sponza, V. Véniard, F. Sottile, C. Giorgetti, and L. Reining, Role of localized electrons in electron-hole interaction: The case of $SrTiO_3$, *Phys. Rev. B* **87**, 235102 (2013).
- [75] X. Zhang, J. A. Leveillee, and A. Schleife, Effect of dynamical screening in the Bethe-Salpeter framework: Excitons in crystalline naphthalene, *Phys. Rev. B* **107**, 235205 (2023).
- [76] J. T. Devreese, S. N. Klimin, J. L. M. van Mechele, and D. van der Marel, Many-body large polaron optical conductivity in $SrTi_{1-x}Nb_xO_3$, *Phys. Rev. B* **81**, 125119 (2010).
- [77] J. C. Phillips, The fundamental optical spectra of solids, *Solid State Physics* **18**, 55 (1966).
- [78] S. K. Tripathy, Refractive indices of semiconductors from energy gaps, *Opt. Mater.* **46**, 240 (2015).
- [79] T. Trupke, M. A. Green, and P. Würfel, Improving solar cell efficiencies by down-conversion of high-energy photons, *J. Appl. Phys.* **92**, 1668 (2002).
- [80] H. Philipp and H. Ehrenreich, Optical properties of semiconductors, *Phys. Rev.* **129**, 1550 (1963).
- [81] Reference Solar Spectral Irradiance: Air Mass 1.5, <http://rredc.nrel.gov/solar/spectra/am1.5/>.
- [82] A. Alkauskas, Q. Yan, and C. G. Van de Walle, First-principles theory of nonradiative carrier capture via multiphonon emission, *Phys. Rev. B* **90**, 075202 (2014).
- [83] J. Buckeridge, Equilibrium point defect and charge carrier concentrations in a material determined through calculation of the self-consistent fermi energy, *Comput. Phys. Commun.* **244**, 329 (2019).
- [84] J.-H. Yang, L. Shi, L.-W. Wang, and S.-H. Wei, Non-radiative carrier recombination enhanced by two-level process: a first-principles study, *Sci. Rep.* **6**, 1 (2016).
- [85] S. Kim, J.-S. Park, S. Hood, and A. Walsh, Lone-pair effect on carrier capture in Cu_2ZnSnS_4 solar cells, *J. Mater. Chem. A* **7**, 2686 (2019).
- [86] D. Dahliah, G. Brunin, J. George, V.-A. Ha, G.-M. Rignanese, and G. Hautier, High-throughput computational search for high carrier lifetime, defect-tolerant solar absorbers, *Energy Environ. Sci.* **14**, 5057 (2021).
- [87] J. S. S. Park, S. Kim, Z. Xie, and A. Walsh, Point defect engineering in thin-film solar cells, *Nat. Rev. Mater.* **3**, 194 (2018).
- [88] A. Alkauskas, C. E. Dreyer, J. L. Lyons, and C. G. Van de Walle, Role of excited states in Shockley-Read-Hall recombination in wide-band-gap semiconductors, *Phys. Rev. B* **93**, 201304(R) (2016).